Physics of Fluids

RESEARCH ARTICLE | OCTOBER 16 2024

Investigation of streamwise streak characteristics over a compression ramp at Mach 4

Guoqin Zhao (赵国钦); Tianju Ma (马天举); Zongnan Chen (陈宗南); Zijian Zhang (张子健);
Jiaao Hao (郝佳傲); Chih-Yung Wen (温志湧)

Physics of Fluids 36, 104121 (2024)
https://doi.org/10.1063/5.0224568

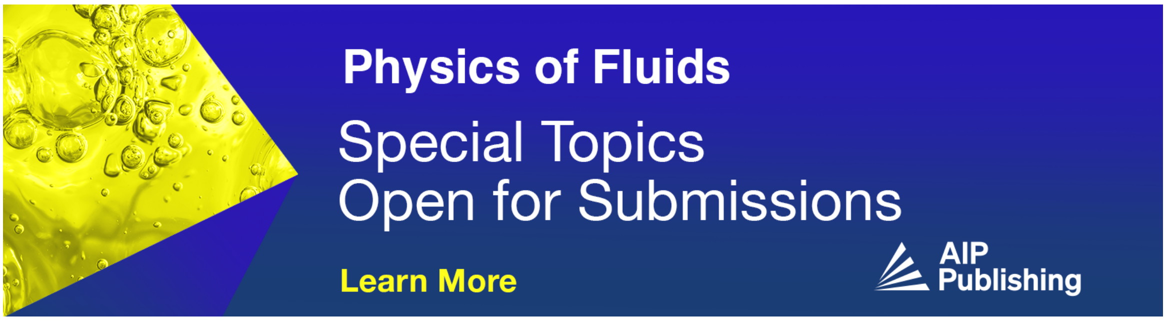

AIP Publishing

Physics of Fluids ARTICLE pubs.aip.org/aip/pof

Investigation of streamwise streak characteristics over a compression ramp at Mach 4

Cite as: Phys. Fluids **36**, 104121 (2024); doi: 10.1063/5.0224568
Submitted: 21 June 2024 · Accepted: 6 September 2024 ·
Published Online: 16 October 2024

Guoqin Zhao (赵国钦),[1] **Tianju Ma (马天举),**[2] **Zongnan Chen (陈宗南),**[1,3,a)] **Zijian Zhang (张子健),**[1] **Jiaao Hao (郝佳傲),**[1] **and Chih-Yung Wen (温志湧)**[1]

AFFILIATIONS

[1]Department of Aeronautical and Aviation Engineering, The Hong Kong Polytechnic University, Hong Kong, China
[2]Academy of Aerospace Propulsion Technology, Shaanxi 710100, China
[3]School of Aerospace Engineering, Beijing Institute of Technology, Beijing 100081, China

[a)]Author to whom correspondence should be addressed: zongnan.z.chen@polyu.edu.hk

ABSTRACT

Experiments of shock wave/boundary layer interactions over a nominally two-dimensional compression ramp are conducted in a Mach 4 Ludwieg tube tunnel. Measurements of Schlieren, Rayleigh scattering, and surface pressure are performed to present the relevant flow features. The effects of two parameters, namely the Reynolds number based on the length of the flat plate and the ramp angle, on the flow stabilities are focused on. Four ramp angles of 6°, 8°, 10°, and 12° are tested under a Reynolds number of 7.22×10^5, while two other Reynolds numbers (3.66×10^5 and 9.19×10^5) are investigated with a ramp angle of 10°. Streamwise streaks are observed downstream of the reattachment point. The spanwise wavelength of the streaks remains unchanged with different ramp angles, whereas it slightly decreases as the Reynolds number increases. Power spectral density results show that the flow is transitional in the streak region and becomes turbulent where streaks break down. When increasing the ramp angle or the Reynolds number, the streamwise length of streaks shrinks. Two different patterns are distinguished at the breakdown, resembling the two unstable modes observed in the breakdown of Görtler vortices. To clarify the underlying physics of the formation of streaks, global stability analysis and resolvent analysis are carried out. Two regions of maximum optimal gain are identified, which are associated with Mack's first mode and streaks. The former can serve as an initial seed of Görtler instability via nonlinear interaction, while the latter can be associated with transient growth due to the lift-up mechanism and Görtler instability.

I. INTRODUCTION

Shock wave/boundary layer interactions (SWBLIs) are commonly encountered in supersonic and hypersonic flows, which create difficulty in the design of aerodynamic configurations and propulsion systems of high-speed flight vehicles. The adverse pressure gradient in SWBLIs distorts the velocity profile of the boundary layer, resulting in significant changes in the entire flow-field structure, including the formation of separation bubbles and streamwise vortices.[1] Moreover, the mechanisms of flow instability and the laminar–turbulent transition process can be fundamentally different from those of the unseparated flow. In practice, SWBLIs can pose severe problems for those vehicles, including a loss of maneuverability, peaks in surface thermomechanical loadings, enhanced pressure loss, and an unsteadiness-induced adverse structural response.[2] Therefore, numerous investigations[3–5] have been conducted over the past century to reveal the physical mechanism underlying these phenomena.

The physics of SWBLIs have been examined in multiple model configurations, such as compression corner,[6–8] double cone,[5,9] oblique shock wave incidence,[10,11] hollow cylinder/flare,[12,13] etc. Among them, the compression corner configuration is widely applied in air vehicles such as control surfaces, inlets of engines, and junctions.[14] The study on SWBLIs on this configuration is significant and many questions regarding the transition to turbulence process remain to be answered, e.g., the origin of the streamwise streaks that appear on this nominal two-dimensional (2D) construction, the evolution and breakdown of streamwise streaks, etc.

The first observation of streamwise streaks is traced back to the early work of Ginoux[15] in 1969 using a hollow cylinder/flare model. Subsequently, numerous scholars have endeavored to elucidate the origin and evolution of streamwise streaks, which can manifest as variations in spanwise surface heat flux, wall pressure, etc. Simeonides and Haase[16] noticed that the streamwise streaks were closely linked to the laminar–turbulent transition process since the streaks commenced in the vicinity of the reattachment region and disappeared when the fully turbulent flow was formed. Similar observations have been documented by Lugrin *et al.*[17] Infrared thermography was employed by De Luca *et al.*[18] and De La Chevalerie *et al.*[19] to examine the effects of the unit Reynolds number and ramp angle on the streamwise streaks in a Mach 7.14 compression corner flow, which covered a wide range from laminar to transitional interactions. However, the mechanisms behind are still not clear, such as the relation with the transition process as well as the origin of the streaks.

The transition process is far from being understood in supersonic flows due to its complexity. Reshotko[20] summarized five paths that lead to transition, including eigenmode growth, transient growth, bypass mechanisms, etc. In practice, modal growth is often observed under low environmental disturbances. Therefore, multiple instability modes have been identified to explain the propagation and amplification of disturbances,[21,22] which is often referred to as convective instability. However, intrinsic instability, also known as global instability, has the potential to trigger the transition process without external pertubations.[23,24] It is well known that the separated flow in SWBLIs can support both convective and global flow instabilities. In the case of weakly separated flows, global instability may be absent, which indicates a globally stable status.[25] However, the flow becomes globally unstable when increasing the interaction strength.[7] From a global stability perspective, a flow is referred to as an oscillator if it is globally unstable, otherwise, it is called a noise amplifier.[26] Therefore, global instability possesses an intrinsic nature, while convective instability amplifies the disturbances and propagates them downstream. Hao *et al.*[7] established a criterion based on a scaled ramp angle to predict the stability boundary for hypersonic compression corner flows. Benitez *et al.*[27] investigated the flow instability on a sharp cone-cylinder-flare model in the Boeing/AFOSR Mach 6 quiet tunnel (BAM6QT). They found evidence of convective instability generated by shear layers under quiet flows. However, they also noticed global instability dominates when experiments are run at conventional noise conditions where the waves detected by PCB pressure sensors become local oscillations. Balakumar *et al.*[28] investigated a 2D compression ramp flow at Mach 5.373 and analyzed the evolution of second mode disturbances with the absence of global instability. The exponential growth of perturbations has been observed both upstream and downstream of the separated region while remaining neutral across the separated region. In addition, the transient growth can also be significant in some scenarios.[29,30]

Concerning the origin of the streaks, the streaks are traditionally considered as the footprint of Görtler-like vortices.[31] However, recent studies have proposed different explanations based on a deeper understanding of flow instabilities. For example, Cao *et al.*[24] reported that the occurrence of streamwise streaks downstream of reattachment is triggered by intrinsic instability in the flow system. Similarly, Sawant *et al.*[32] reported that the origin of global instability was traced in the flow region of interaction of the separation shock and the bubble, which resulted in the formation of streaks. Dwivedi *et al.*[33] employed resolvent analysis to examine the amplification of external disturbances in compression ramp flows at Mach 8. They observed that the dominant output takes the form of steady streamwise streaks at the reattachment region, and further explained that the baroclinic effect plays an important role in the formation of streamwise streaks. Lugrin *et al.*[8] found that the streaks can originate from both convective and global instability mechanisms. More recently, Hao *et al.*[30] found that the amplification mechanisms of the streamwise streaks near the reattachment region are mainly Görtler instability.

Despite these efforts, many questions regarding the origination of streamwise streaks and their evolution remain worth a further study. Most of the previous experimental studies focus on the footprint of the streamwise vortices to observe their characteristics, such as the thermal streaks measured by an infrared camera, which are the time-averaged information lacking the transient details. The streamwise vortex itself was rarely observed directly, especially the visualization of its evolution and breakdown process to turbulence. To gain a deeper understanding of streamwise streak characteristics, the present study investigates a supersonic laminar flow over a compression corner using a combination of experiments, numerical simulations, and theoretical analysis, to determine the transition process on the ramp and the origination of streamwise streaks.

In addition, Mach number changes both the strength of the shock and boundary layer profile in SWBLI flows. From the supersonic to hypersonic regime, the physics and mechanisms of instability that dominate in the flow field are known to be different. For instance, Mack[34] found that the oblique wave is most unstable when the Mach number is less than 4, which is known as Mack's first mode. Mack's second mode emerges when the Mach number is greater than 2.2 and dominates in the hypersonic flows. Table I presents the relevant

TABLE I. Research on the flow instability in SWBLI over compression ramp.

	Geometry	M_∞	Method	Instability involved
Benitez *et al.*[36]	Cone–cylinder–flare	6	EXP[a]	Shear-layer mode, second mode
Hao *et al.*[30]	Compression ramp	7.7	CFD[b]	Second mode, streak mode
Li and Hao[13]	Hollow cylinder–flare	2.25	CFD	Global instability
Niessen *et al.*[37]	Compression ramp	1.7	CFD	Convective instability
Butler and Laurence[38]	Cone–flare	6	EXP	Second mode
Cao *et al.*[24]	Compression ramp	7.7	CFD	Global instability
Lugrin *et al.*[8]	Hollow cylinder–flare	5	EXP	Shear-layer mode, global instability
Paredes *et al.*[39]	Cone–cylinder–flare	6	CFD	First mode, second mode, and global instability
Dwivedi *et al.*[33]	Compression ramp	8	CFD	Baroclinic effect
Roghelia *et al.*[6]	Compression ramp	7.7	EXP	Görtler instability

[a] Experiment.
[b] Computational fluid dynamics.

research on the flow instability in SWBLI over compression ramp in recent years. It is noted that most studies focus on the instability of hypersonic flows as well as low supersonic Mach number flows, while few have investigated flows at moderate supersonic Mach numbers. In a Mach 4.5 flat-plate boundary layer, Mack's first mode, second mode, and the streak mode may occur, as reported by Bugeat *et al.*[35] Yet, the instability characteristics of SWBLI over compression ramp under supersonic flow (Mach number less than 5) has been relatively underexplored, especially experimentally, which addresses the need to acquire more experimental data and inquire into a more in-depth understanding of flow instability at those conditions.

In general, the present study provides details of the streamwise streaks from emerging to breakdown over the compression ramp at Mach 4, which is the first time to be observed directly by Rayleigh scattering, contributing an extended experimental dataset for future research. Analytical tools, including global stability analysis (GSA) and resolvent analysis, are employed to investigate the underlying physics. The remaining parts of this paper are organized as follows: The experimental setup and model configuration are introduced in Sec. II. Section III provides the details of numerical methods, including the base flow solver, GSA, and resolvent analysis. In Sec. IV, the general features of SWBLIs on a compression corner are first discussed. Then, the visualization of the transition that occurs on the ramp is captured by Rayleigh scattering, and the effects of ramp angle and Reynolds number are analyzed in detail. The relationship between the transition process and the breakdown of streamwise streaks is further discussed. Eventually, GSA and resolvent analysis are employed complementarily to investigate the origination of streamwise streaks observed in experiments. Finally, a conclusion is provided in Sec. V.

II. EXPERIMENTAL SETUP

A. Experimental facilities and flow conditions

The experiments were conducted in a Mach 4 Ludwieg tube tunnel at the Hong Kong Polytechnic University.[40] As shown in Fig. 1, it primarily consists of a gas storage section, a Mach 4 converging–diverging nozzle, a test section, and a dump tank. During the experiment, the gas storage section is charged with pressurized air, and the nozzle, the test section, and the dump tank is vacuumed. The supersonic flow is initiated via the burst of a diaphragm between the gas storage section and the nozzle when the critical pressure difference is reached. The diameter of the nozzle exit is 315 mm. The tunnel has a quasi-steady test time of up to 40 ms. The free-stream Mach number M_∞ is 4.02 ± 0.02. The free-stream noise level is determined in the form of $p'_{0,rms}/\bar{p}_0$, where $p'_{0,rms}$ and $\bar{p}_0$ represent the root mean square (RMS) of the fluctuation and the mean of the stagnation pressure measured by the Kulite sensors mounted in the pitot tube. In the current wind tunnel, the free-stream noise level is around 1.5%, which is in the typical range for a conventional Ludwieg wind tunnel.[41–43] Based on the power spectral density (PSD) analysis of the dynamic pressure measured by the pitot tube, the absence of discernible frequency peaks in the PSDs unequivocally suggests the lack of specific frequency-related noise within the freestream. Note that, the free-stream noise has a significant effect on flows. As reported by Threadgill *et al.*,[44] the specific noise peak could impact the development of convective modes within the same frequency range, and then promote the transition process. Yet, the aforementioned PSD results show that no specific frequency peak is observed, indicating that the noise has a limited effect on the promotion to a higher amplitude in the convective modes. Moreover, all experiments are conducted at the same noise level in the present study, making it reasonable to compare changes between different cases. In the present study, the Reynolds number is varied from 3.66×10^5 to 9.19×10^5 based on the characteristic length of the flat plate L (100 mm) by adjusting the thickness of the diaphragm.

B. Model geometry and instrumentation

As shown in Fig. 2(c), the compression corner model is installed at the test section just downstream of the nozzle exit, which consists of a flat plate and a ramp plate with a length of 100 and 250 mm, respectively [see Fig. 2(a)]. The spanwise length of the model is 200 mm, which is long enough and causes limited effects on the flows under the parameters studied in this research.[6,16,45] The coordinate system is constructed with the origin located at the leading edge of the flat plate [see Fig. 2(a)]. The x-axis is coincident with the flow direction, and the y-axis points in the vertical direction. The surface roughness of the two plates is polished to $Ra = 0.2\ \mu$m, and the radius of the sharp leading edge is 0.01 mm. The ramp angle θ can be adjusted from 0° to 30° with an interval of 1°. In the present study, experiments were

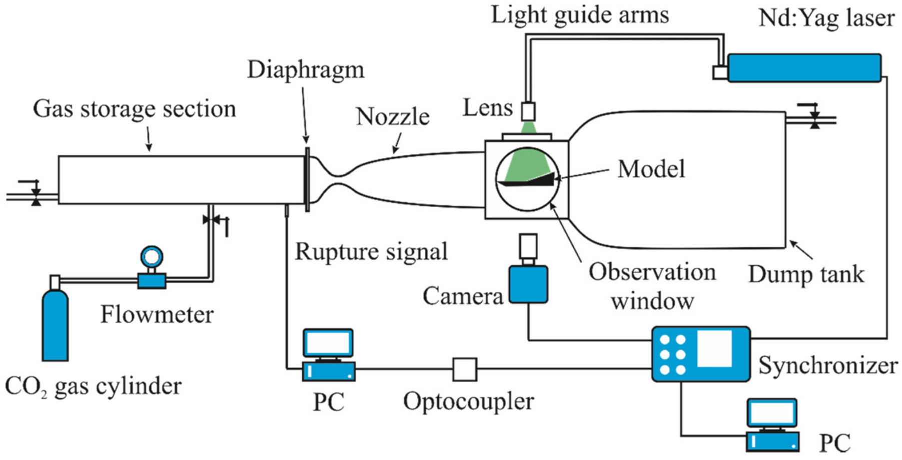

FIG. 1. The schematic of the Ludwieg tube tunnel and the Rayleigh scattering image system.

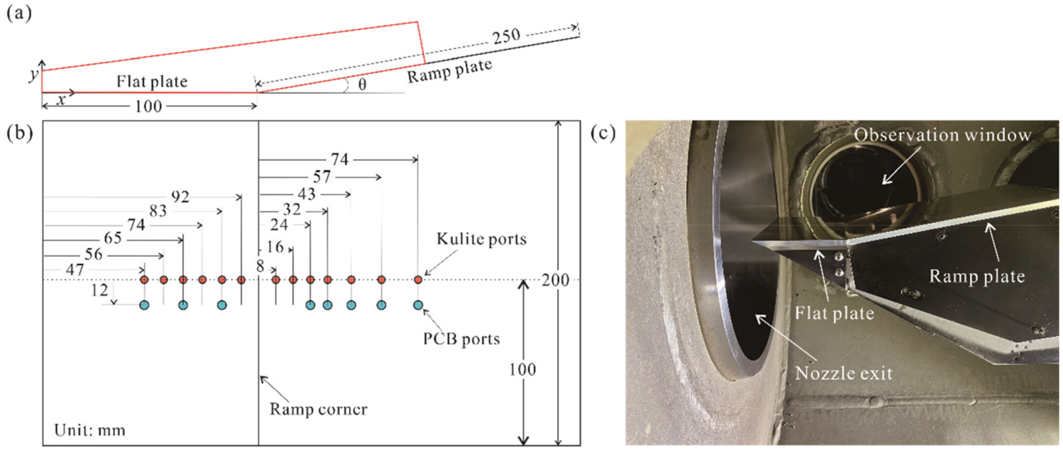

FIG. 2. (a) Schematic of compression corner configuration where Red lines represent the boundary of the computational domain. (b) Locations of the PCB and Kulite pressure sensors in the model, where red circles and green circles indicate where Kulite and PCB sensors are mounted, respectively. (c) Pictures of compression ramp model installed in the wind tunnel.

conducted with ramp angles at 6°, 8°, 10°, and 12°. The parameters of each case tested in experiments are shown in Table II.

A total of 21 pressure ports are positioned at the center region of both plates, measuring the pressure distribution on the model surface. The transducers are flush mounted in the model, guaranteeing the maximum ratio of the roughness height (k) over the thickness of the boundary layer (δ_k) is less than 0.17. Based on Chuvakhov *et al.*'s work,[46] the effects caused by natural disturbances may be stronger than roughness elements when k/δ_k is less than 0.2. Therefore, the roughness of transducers in the present study has a limited effect on the flow structures. The Kulite sensors (XCE-093-5A) are mounted along the central line to measure the static pressure at the surface, with an operational range of 35 ± 0.1 kPa. The diameter of the sensors is 2.4 mm. Those sensors are connected to a DC power supply (TTI QL355P) delivering a constant 10 V voltage. PCB pressure sensors (132B38) are positioned on one side of the Kulite sensors to measure the pressure disturbances, as shown in Fig. 2(b). The diameter of the PCB sensors is 3.18 mm, while the resolution is 7 Pa. PCB sensors are conditioned by an 8-channel signal conditioner 483C05 before being connected to the NI DAQ device. The frequency response is from 11 kHz to 1 MHz. It should be noted that Ort and Dosch[47] found that these PCB sensors have a 300 kHz resonance frequency, which is part of the sensor dynamics. Therefore, the frequency characteristic of the flow disturbances below 300 kHz is considered only in the present study. The voltage signals are acquired by NI PXIe-6368 I/O devices built in a PXIe-1071 PXI chassis with a sampling frequency of 2 MS/s. All these signals are converted to pressure values in the LabVIEW program.

TABLE II. Parameter settings in experiments.

	P_∞ (kPa)	ρ_∞ (kg/m^3)	Re_L ($\times 10^5$)	θ (°)
Case 1	80	0.026	3.66	10
Case 2	159	0.051	7.22	10
Case 3	201	0.065	9.19	10
Case 4	159	0.051	7.22	6
Case 5	159	0.051	7.22	8
Case 6	159	0.051	7.22	12

C. Schlieren setup

A Z-type Schlieren system is set to visualize the flow structures around the compression corner. The shock structures and the separation bubble can be captured clearly to estimate the location of the separation and reattachment point. The system is composed of a xenon lamp with an intensity of up to 300 mW/cm^2 and a high-speed camera (FASTCAM SA-Z type 2100 K-M-32GB) with Nikon Nikkor micro-lens (105 mm *f*1:2.8*D*). The optical path traversing the test section aligns with the model. A knife edge was placed horizontally to visualize the density gradients normal to the modal surface, which is well suited for the low-angled shock/expansion waves.[48] Images are taken at a frame rate of 20 kHz with a resolution of 1024 × 1024 pixels, while the spatial resolution of it is 0.11 mm/pixel.

D. Rayleigh scattering image measurement

In the present study, a Rayleigh scattering technique is employed to visualize the detailed instantaneous flow structures, which avoids the optical ray integration effect occurred in Schlieren images. The schematic is shown in Fig. 1. This system is composed of a Nd: Yag laser, a CCD camera, a computer, a synchronizer, and a CO$_2$ gas cylinder. This laser as the lighting source (Vlite-500) has a wavelength of 532 nm, operating at a pulse energy of around 250 mJ (50% of maximum) and a pulse width of 6 ns. The laser beam traverses a light guide arm and a lens assembly, forming a laser sheet with a thickness of less than 0.5 mm within the field of view (FOV). The lens assembly comprises a convex lens and a cylindrical concave lens. Then, the tracer particles will be lightened by the laser sheet and captured by the CCD camera (FlowSense FCX 24M-30) with a resolution of 5312 × 4600 pixels. The camera is equipped with a 60 mm *f*/2.8D lens to keep an appropriate FOV through the side observation window. In this study, the spatial resolution of FOV is about 35.7 pixels/mm. Note that, due to the laser frequency of up to 15 Hz, only a pair of images can be obtained during the test time. The synchronizer (BNC Delay Pulse Generator 575-8C) is employed to synchronize the laser, CCD camera, and the burst of the diaphragm.

The CO_2 gas is injected into the gas storage section before the burst of the diaphragm. Its volume fraction is controlled at around 1%–2% volume fraction via a flowmeter to achieve the best visualization. Because the free-stream static temperature is near 70 K, the CO_2 gas condenses to tiny solid particles in the freestream. As the diameters of the solid CO_2 particles are much smaller than the wavelength of the laser, it is a kind of Rayleigh scattering.[49] The particles scatter under the illumination, and the scattering light is captured by the camera as the bright region in the image. While the particles move to the boundary layer region, they sublimate to gas due to the relatively high static temperature near the wall, forming a dark region in the images.[50] Therefore, a condensation line appears to distinguish the boundary layer region (dark region) and the main flow region (bright region). In addition, downstream of the shock wave, the density and pressure of the flow increase significantly, resulting in a higher concentration of CO_2 particles there. A difference in luminance can be observed to distinguish the location of the shock wave as well. Note that, the condensation of CO_2 will release heat, which will cause entropy spots. To minimize the heat release in the condensation process, CO_2 is used rather than H_2O as the latter exhibits much higher heat release during the phase transition.[51] In addition, the lower condensation temperature gives CO_2 another advantage as it could delay the onset condensation process, potentially producing smaller particles.

In the present study, two laser sheet planes are strategically deployed to visualize the flow structure, as depicted in Fig. 3. The FOV A is configured parallel to the ramp plate with the distance between the laser sheet and the ramp surface of about 1 mm. Due to the optimal clarity of imaging at the laser focus, the field of view is constrained and set in the centerline region with a dimension of 68 × 125 mm. FOV B is positioned perpendicular to the ramp plate, aligned along the centerline in the streamwise direction. In addition, the weak Mach waves that may be generated at the corners of the leading edge and propagate toward the centerline should be taken into consideration as they may contaminate the flow. In this study, the model spanwise width is long enough and the FOV A is outside of the Mach lines caused by the leading edge corner, which is thus unaffected by the weak Mach waves.

III. NUMERICAL METHODS

To explain the underlying physics of the experimental observations and further analyze the flow instability characteristics, numerical simulation as well as analytical analysis tools, such as GSA and resolvent analysis, have been employed. The governing equations and the details of numerical methods are briefly introduced below.

A. Flow solver

The compressible Navier–Stokes equations for a calorically perfect gas are used in the present study, as follows:

$$\frac{\partial \boldsymbol{U}}{\partial t} + \frac{\partial \boldsymbol{F}_j}{\partial x_j} = \frac{\partial \boldsymbol{F}_{v,j}}{\partial x_j}, \tag{1}$$

where $\boldsymbol{U} = (\rho,\ \rho u_i,\ \rho e)^{\mathrm{T}}$ is the vector of conservative variables. $\boldsymbol{F}_j$ and $\boldsymbol{F}_{v,j}$ denote the vectors of inviscid and viscous fluxes. ρ, u_i, and e represent the density, three components of velocity, and the total energy per unit mass, respectively. The perfect gas equation is employed to make governing equations closed.

The base flow simulation is performed in an in-house multi-block parallel finite-volume solver called PHAROS.[7] The inviscid fluxes are calculated by an approximate Riemann solver, Harten–Lax–van Leer–Contact scheme, and the viscous fluxes are calculated by the second-order central difference. The implicit line relaxation method is employed for the time iteration. The computational domain is illustrated in Fig. 2(a). The grid convergence is determined for a steady state (see the Appendix). As for the boundary layer conditions, the free-stream conditions are applied to the upper and left boundaries, which are identical to the experimental free-stream conditions. At the outflow boundary, a simple extrapolation outflow condition is employed. Isothermal ($T_{\mathrm{w}} = 297$ K) and no-slip conditions are used for the wall.

B. Global stability analysis

The vector of conservative variables $\boldsymbol{U}$ can be decomposed into a steady solution $\boldsymbol{U_{2D}}$, and a small-amplitude perturbation $\boldsymbol{U}'$ as

$$\boldsymbol{U}(x,y,z,t) = \boldsymbol{U}_{2-\boldsymbol{D}}(x,y) + \boldsymbol{U}'(x,y,z,t). \tag{2}$$

Subsequently, the linearized Navier–Stokes equations (LNS) can be obtained by substituting Eq. (2) into Eq. (1) and neglecting the higher order terms. To consider the perturbation term $\boldsymbol{U}'$, we assume it to be spanwise periodic as

$$\boldsymbol{U}'(x,\ y,\ z,\ t) = \widehat{\boldsymbol{U}}(x,\ y)\exp\left[i\frac{2\pi}{\lambda}z - i(\omega_r + i\omega_i)t\right], \tag{3}$$

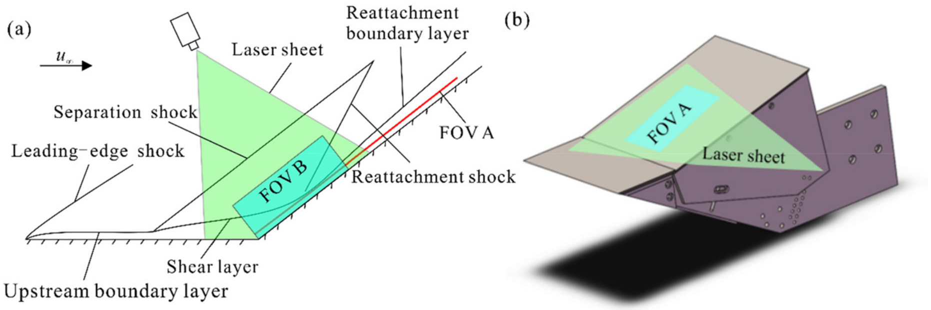

FIG. 3. (a) The schematics of the laser sheets and the FOV A and B in the Rayleigh scattering experiments. (b) FOV A in a three-dimensional view.

where $\widehat{\boldsymbol{U}}$ denotes the 2D eigenfunction, while λ, ω_i, and ω_r are the spanwise wavelength, the growth rate, and the angular frequency, respectively. A positive growth rate ω_i represents that the flow is globally unstable. $\omega_r = 0$ represents a stationary mode, while a non-zero ω_r indicates an oscillatory mode. When substituting Eq. (3) into LNS, we can transform the linearized stability problem into an eigenvalue problem. The eigenvalue problem is then solved by the implicit restarted Arnoldi method implemented in ARPACK[52] for a given λ. The lower–upper decomposition implemented in Super-LU[53] is used to efficiently explore the eigenvalue spectra.

C. Resolvent analysis

Resolvent analysis is employed to investigate the behavior of the flow as a noise amplifier, where an external small-amplitude disturbance is introduced. Note that only globally stable flow is considered, which means all the temporal growth of disturbances will decay to zero over time. The LNS is expressed as

$$\frac{\partial \boldsymbol{U}'}{\partial t} = \boldsymbol{A}\boldsymbol{U}' + \boldsymbol{B}\boldsymbol{f}', \tag{4}$$

where $\boldsymbol{A}$ is the Jacobian matrix evaluated using the base flow, while $\boldsymbol{B}$ constrains the forcing to a localized region. In the present study, the forcing is specified at $x/L = 0.2$ as

$$\boldsymbol{f}'(x, y, z, t) = \widehat{\boldsymbol{f}}(x, y)\exp(i\beta z - i\omega_r t), \tag{5}$$

which is harmonic in time as well as in the spanwise direction. The long-time solution of Eq. (4) takes the same form as the forcing, which is expressed as

$$\boldsymbol{U}'(x, y, z, t) = \boldsymbol{U}'(x, y)\exp(i\beta z - i\omega_r t). \tag{6}$$

Then, substituting Eq. (5) and Eq. (6) into Eq. (4), and discretizing the linearized equation in the same way as in the GSA, gives

$$\widehat{\boldsymbol{U}} = \boldsymbol{R}\boldsymbol{B}\widehat{\boldsymbol{f}}, \quad \boldsymbol{R} = \left(-i\omega_r \boldsymbol{I} - \boldsymbol{A}\right)^{-1}, \tag{7}$$

where $\boldsymbol{R}$ and $\boldsymbol{I}$ are the resolvent matrix and identity matrix, respectively. The objective of the resolvent analysis is to find the forcing and response pair that maximizes the energy amplification. This maximum amplification is referred to as the optimal gain, which is defined by

$$\sigma 2(\beta, \omega_r) = \max_{\widehat{f}} \frac{\left\|\widehat{\boldsymbol{U}}\right\|_E}{\left\|\boldsymbol{B}\widehat{\boldsymbol{f}}\right\|_E}. \tag{8}$$

The Chu energy[54] is used to evaluate the energy norm as

$$\left\|\widehat{\boldsymbol{U}}\right\|_E = \widehat{\boldsymbol{U}}^* \boldsymbol{M}\widehat{\boldsymbol{U}}, \tag{9}$$

where the superscript * represents the complex conjugate and the weight matrix is denoted as $\boldsymbol{M}$.[35] The optimization problem is transformed into an eigenvalue problem[35] by

$$\boldsymbol{B}^*\boldsymbol{M}^{-1}\boldsymbol{R}^*\boldsymbol{M}\boldsymbol{R}\boldsymbol{B}\widehat{\boldsymbol{f}} = \sigma^2\widehat{\boldsymbol{f}}. \tag{10}$$

For a given β and ω_r, the eigenvalue problem can be solved using ARPACK, which is a similar process in the GSA.

IV. RESULTS

A. General flow features over a supersonic compression corner

First, the general flow features of the mean flow over a supersonic compression corner are examined. Figure 4(a) illustrates a typical Schlieren image of SWBLIs over the compression ramp at a 10° ramp angle with $Re_L = 7.22 \times 10^5$, which can be seen as a representative for all cases. The Schlieren image is time-averaged by 300 instantaneous images in the period of steady flow taken by a high-speed camera at a frame rate of 20 kHz. Due to the sufficiently large pressure increase induced by the presence of the ramp, the boundary layer on the flat plate separates from the surface and then reattaches to the downstream ramp, leading to a separation shock and a reattachment shock at the separation and reattachment points, respectively. These can be observed clearly in Fig. 4(a), where the separation and reattachment points determined from the Schlieren images are indicated by open circles. Note that the true separation and reattachment points are defined by zero skin friction coefficient, which is difficult to be obtained in the present experiments. Hence, in the present study, the separation point is extrapolated from the intersection of the separation shock and the plate surface, while the reattachment point is extrapolated from the intersection of the reattachment shock and the shear layer. To make it consistent, the same criterion is applied to the numerical results. Between them, a recirculation zone forms beneath the separated shear layer, which is normally referred to as a separation bubble.

In Fig. 4(a), the leading edge shock induced by the flat plate can be observed, though the leading edge of the flat plate is outside of the FOV. In the present study, the boundary layer remains laminar upstream of the separation point. In Fig. 4(b), the same main flow structures, such as the separation shock and the separation bubble, are captured by the Rayleigh scattering technique, which illustrates the instantaneous flow structures. In addition to the main flow structures, the transition downstream of the reattachment region can be observed clearly, which will be discussed in more detail later.

Figure 5 compares the surface pressure coefficients obtained from the Kulite sensors in the experiments with those from DNS at the 6° and 10° ramp angles and $Re_L = 7.22 \times 10^5$. The surface pressure coefficient C_p is defined by

$$C_p = \frac{p_w}{0.5\rho_\infty u_\infty^2}, \tag{11}$$

where p_w indicates the pressure at the surface. The surface pressure coefficient C_p obtained by DNS shows that the pressure at the wall surface experiences a steep increase near the separation region followed by a pressure plateau. Downstream of the corner, surface pressure rises again. When the ramp angle increases [see Fig. 5(b)], the separation point moves upstream accompanied by a steeper pressure rise, which leads to a larger separation region. In experimental results, a similar trend can be observed, although there are some deviations when compared with numerical results. A general agreement can be achieved in Fig. 5(a), where the ramp angle is small. However, the discrepancy is more apparent at a larger ramp angle, which will be explained later. Note that the error bar of experimental data is calculated by the standard deviations of static pressure.

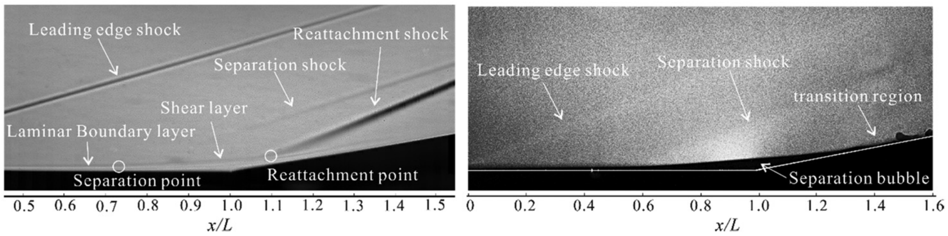

FIG. 4. (a) Time-averaged Schlieren image and (b) Rayleigh scattering image of SWBLIs (instantaneous results) over compression corner at 10° ramp angle with $Re_L = 7.22 \times 10^5$.

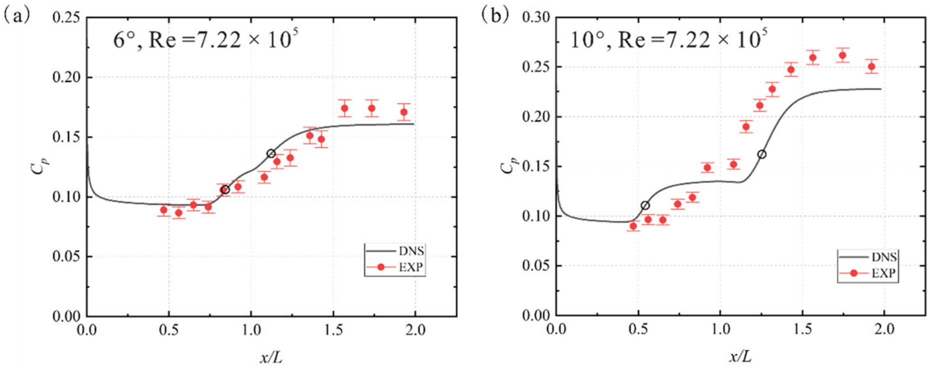

FIG. 5. Surface pressure coefficients of experiments and DNS at ramp angles of (a) 6° and (b) 10° and $Re_L = 7.22 \times 10^5$. The separation and reattachment points obtained from 2D DNS base flows are denoted by open circles.

B. Transition on the ramp

In this section, the effects of ramp angle and Reynolds number as well as the transition process that occurs on the ramp are discussed.

1. Effects of ramp angle

The locations of separation points determined by Schlieren images in all cases are presented in Table III, compared with numerical Schlieren results obtained from 2D DNS base flow. The cause of the difference between experiments and numerical simulation is discussed later (see Sec. IV D). First, we focus on the effects of ramp angle. While increasing the ramp angle, the separation point gradually moves upstream, enlarging the size of the separation bubble, as shown in Fig. 6. To be specific, when the ramp angle is at 6°, the separation occurs at the location of $x/L = 0.77$, while it shifts toward the leading edge at $x/L = 0.62$ as the ramp angle increases to 12°. In terms of the length from the separation point to the corner, it extends from 23 mm at the ramp angle of 6° to 38 mm at 12°, indicating a 65% rise in length. Similarly, the reattachment points shift downstream as the ramp angle increases, although the change is not as significant as at the separation point. As a result, a monotonic increasing trend in the size of the separation bubble can be observed while increasing the ramp angle, which resembles typical behavior in laminar SWBLI flow. Similar observations were made by Gai and Khraibut[55] in the numerical simulation under laminar flow at Mach 9.1, using a compression corner geometry. Note that if the incoming flow were transitional, a reverse trend could be observed.[8,56] In addition, the inclined angle of separation shock shows a slight increase as well while increasing the ramp angle.

TABLE III. The locations of separation and reattachment points in different cases.

			Separation point (x/L)		Reattachment point (x/L)	
	θ (°)	Re_L ($\times 10^5$)	Exp.	DNS	Exp.	DNS
Case 1	10	3.66	0.74	0.62	1.12	1.26
Case 2	10	7.22	0.70	0.56	1.11	1.26
Case 3	10	9.19	0.67	0.53	1.11	1.27
Case 4	6	7.22	0.77	0.84	1.08	1.13
Case 5	8	7.22	0.74	0.72	1.12	1.23
Case 6	12	7.22	0.62	0.45	1.17	1.29

An intriguing finding made by the Rayleigh scattering technique is the presence of streamwise streaks. As shown in Fig. 7, the FOV is focused on the ramp plate where the laser sheet is parallel to it. The distance between the laser sheet and the ramp surface is about 1 mm, obtaining instantaneous flow structures within the boundary layer downstream of the reattachment point. The reattachment lines denoted by the red lines are determined by Schlieren images. The streaks are observed downstream of the reattachment region at all ramp angles, which are essentially the streamwise vortices in the boundary layer. Similar streak patterns have been observed in previous studies,[50,57] where they associated these streaks with Görtler vortices as well as the transition process. Note that the laser sheet cut through the reattachment boundary layer at the ramp plate, which means the streaks may originate in the shear layer but cannot be traced by this laser sheet because of the warping on the condensation line from the shear layer to the reattachment region. In the current study, the streaks within the transitional region on the ramp plate are focused. For the streaks' origination location, we will further investigate through the visualization of laser sheets crossing the flow direction within the shear layer region in future work.

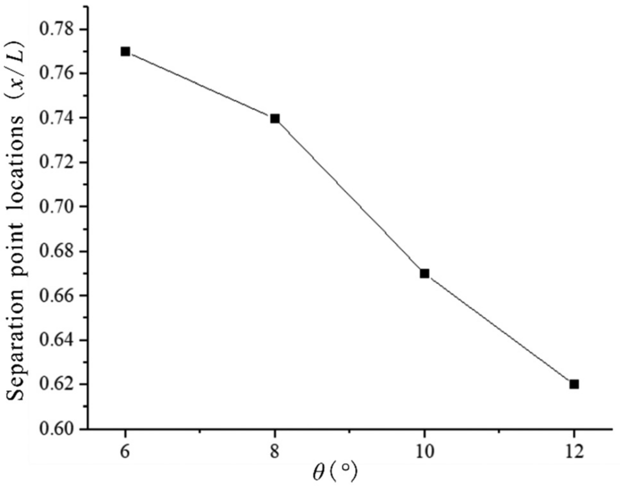

FIG. 6. The relation curve between the locations of separation points and the ramp angles.

The dimension of the images in Fig. 7 is around 68 × 125 mm^2 in spanwise and streamwise directions, respectively. It is clear to see that when the ramp angle is at 6° [see Fig. 7(a)], the streamwise streaks are observed downstream of the reattachment line, approximately at $x/L = 1.22$, and the streamwise vortices extend for a relatively long distance before breaking down into small-scale vortices. When the ramp angle increases to 8°, the streaks occur further upstream. Meanwhile, the mean streamwise length of the streaks decreases from around 55 to 38 mm. Note that the mean streamwise length of streaks is the average length of streaks in the FOV as illustrate in Fig. 7(a), yet there is still some uncertainty in the determination of breakdown position. Subsequently, at the ramp angles of 10° and 12°, the onset of streamwise streaks continue shifting upstream to the reattachment point, and the average length of streaks keeps decreasing to only 28 and 14 mm, respectively. To be specific, in the case of 12° [see Fig. 7(d)], the streamwise streaks appear even upstream of the reattachment line, at around $x/L = 1.11$, and break down very quickly downstream, only persisting a length of around 14 mm. It is noted that the streaks may originate further upstream in the shear layer, which cannot be captured as those structures are outside of the laser sheet plane. The declined trend in the streamwise length of the streaks on the ramp plate is also shown in the previous study[6,46] by the surface heat streaks at Mach 7.7. Roghelia *et al.*[6] considered that three main factors influence the length of the streaks, namely shock strength, shear layer length, and flow curvature. In the present study, with increasing the ramp angle, the shock strength, the length of the shear layer, and flow curvatures at separation and reattachment points increase simultaneously. As a result, the length of the streaks decreases. In terms of the spanwise wavelength of the streaks, which is defined as the distance between two adjacent streaks, the averaged wavelength observed in all ramp angles varies from 3.1 to 3.4 mm. Notably, to achieve experimental repeatability, more than five measurements have been conducted for averaging.

To examine the growth and breakdown of streamwise vortices in more detail, a side view of the instantaneous flow structure using the Rayleigh scattering technique is presented in Fig. 8. The laser sheet is positioned at the center of the plate along the streamwise direction, and the evolution of streamwise vortices can be observed from $x/L = 1.0$ to 1.57 along the ramp. The black region where the solid CO_2 particles sublimate to gas approximately represents the regions of separation bubble and boundary layer, and the red dashed line denotes the location of the reattachment point determined by Schlieren images. When the ramp angle is at 6° [see Fig. 8(a)], the boundary layer shows a small variation for a relatively long distance downstream of the reattachment point, until some bulges appear in the boundary layer at $x/L \approx 1.45$. However, no obvious breakdown of vortices can be seen in the field of view, which indicates the streamwise vortices have not broken down into small-scale vortical structures yet.

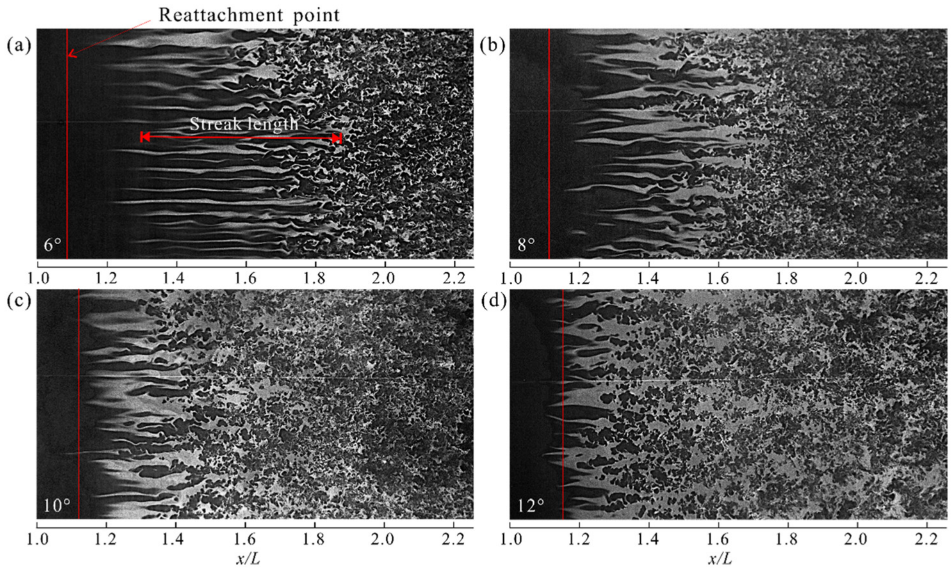

FIG. 7. The spanwise views of Rayleigh scattering images at the ramp plate at (a) 6°, (b) 8°, (c) 10°, and (d) 12°. The flow direction is from left to right. The ramp corner is outside the left bound of the image and the red line represents the reattachment region.

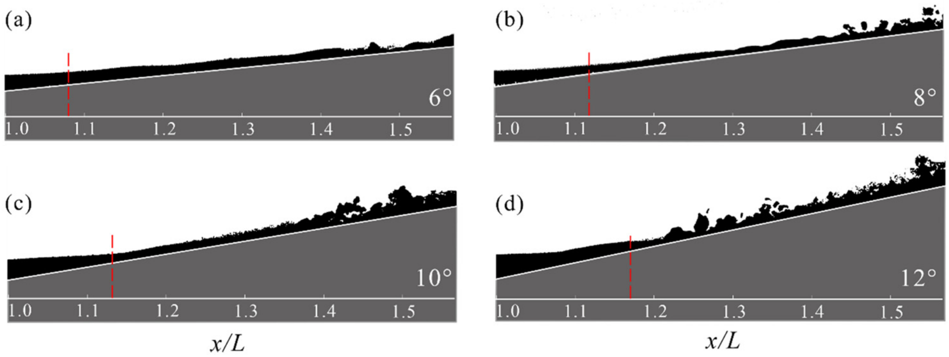

FIG. 8. Rayleigh scattering images from the side view downstream of the corner with ramp angle at (a) 6°, (b) 8°, (c) 10°, and (d) 12°. The red dashed line denotes the location of reattachment point determined by Schlieren images.

In Figs. 8(b) and 6(d), the breakdown process occurs at an earlier stage when increasing the ramp angle, where the small-scale vortices can be observed separated from the streamwise vortices. For example, the breakdown of vortices occurs between $x/L = 1.4$ and 1.5 at an 8° and 10° ramp plate [see Figs. 8(b) and 6(c)], whereas the location of breakdown moves upstream to around $x/L = 1.25$ at a 12° ramp angle [see Fig. 8(d)]. Notably, those bulges observed in the region near the breakdown may be the result of the roll-up process.[50] These bulges, along with the streak pattern in the spanwise direction, exhibit the three-dimensionality of the vortices. Downstream of reattachment, three-dimensional waves evolve, which is accomplished by the low-speed flow lifting up from the wall region and the mainstream flow sweeping down to the boundary layer. Previous studies have investigated the process in incompressible flows[58,59] as well as compressible flows.[50] Summarily, when increasing the ramp angle, a stronger shear layer formed at the edge of the boundary layer, promoting the stretching, twisting, and eventually breakdown of the vortices.

In general, the Rayleigh scattering images from the top view and side view well depict the whole evolution process of streamwise streaks, from the emergence of streamwise vortices to their breakdown. However, it only provides a snapshot of the flow field without the temporal characteristics of the streaks. Therefore, PCB pressure sensors are employed to obtain the pressure fluctuations along the streamwise direction, inspecting the evolution and amplification of the vortices. In the present study, to avoid the impact of the free-stream disturbances in the low-frequency range, the pressure fluctuations were filtered by the bandpass of 100 –300 kHz, as shown in Fig. 9. The signal at the most upstream location is the lowest line in the figure, while the highest line represents the pressure fluctuations at the most downstream location. Each adjacent pressure signal is offset 0.6 kPa for clarity. Nearly no significant high-frequency fluctuations at the flat plate in all cases. The initial small fluctuation packets occur at the first PCB station on the ramp, indicating the onset of the transition process. The intermittency of the pressure fluctuations increases until reaching a saturated state, indicating the flow has transitioned to a turbulent state. In Figs. 9(a) and 7(b), the pressure fluctuations saturated at about $x/L = 1.74$ and 1.57, respectively. As the ramp angle is increased to 10° and 12°, that location moves upstream to about $x/L = 1.43$ and 1.24, respectively. Notably, these locations agree well with those where the streamwise streaks are observed to break down (see Fig. 7).

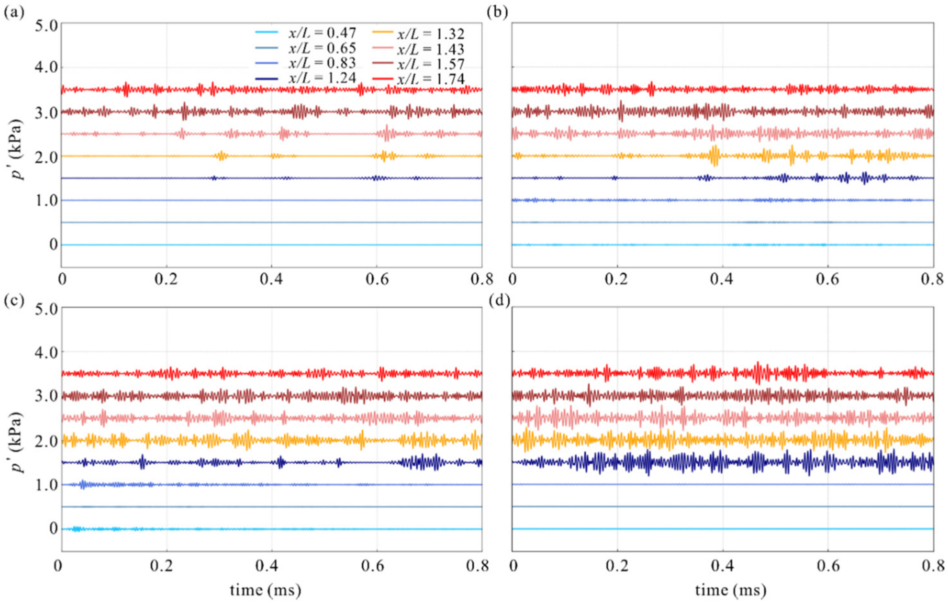

FIG. 9. Time series of pressure disturbance along the streamwise direction in the (a) 6°, (b) 8°, (c) 10°, and (d) 12° ramps with the bandpass of 100–300 kHz.

In summary, the transition process would be significantly affected by the ramp angle. Concerning the streamwise streaks, the streamwise streaks occur downstream of the reattachment point but gradually move upstream when increasing the ramp angle. The same trend can be observed for the breakdown of streaks. Therefore, the streamwise extension of the streaks decreases as the ramp angle increases. Based on the results of the pressure measurement, the region where the streaks occur largely coincides with the transitional region. Additionally, the wavelength of the streamwise streaks does not exhibit a distinct change with variations in the ramp angle.

2. Effects of Reynolds number

As illustrated in Table III, the reattachment point remains nearly unchanged in all cases with different Reynolds numbers, while the separation point moves upstream as the Reynolds number increases. The trend of the separation point is similar to the effects of ramp angle. In consideration of Rayleigh scattering images at the spanwise view of the ramp plate, the effects of the Reynolds number are hereinafter discussed at a fixed ramp angle of 10°. Figure 10 illustrates the streamwise streaks along the ramp plate at Reynolds numbers 3.66×10^5, 7.22×10^5, and 9.19×10^5. The streamwise streaks that were observed instantaneously by the Rayleigh scattering technique all originate near the reattachment region and extend along the flow direction until break down downstream. When $Re_L = 3.66 \times 10^5$, the streamwise streaks appear at around $x/L = 1.25$ and break down at around $x/L = 1.7$, with a mean streamwise transition length of 45 mm. As the Reynolds number increases to 7.22×10^5, the streamwise streaks move upstream and the mean streamwise transition length of streaks decreases as well. When Reynolds number further rises to 9.19×10^5, streamwise streaks appear immediately downstream of the reattachment point at around $x/L = 1.15$ and break down at around $x/L = 1.35$. Hence, the average length of the streaks declines to 20 mm. Therefore, the trend is similar to the effect of ramp angle. The spanwise wavelength at $Re_L = 3.66 \times 10^5$ is around 3.8 mm, while slightly decreasing to 3.4 mm at $Re_L = 7.22 \times 10^5$. When Reynolds number further increases to 9.19×10^5, this value further decreases to 2.9 mm. Therefore, the spanwise wavelength declines as the Reynolds number increases. This declining trend has also been reported in previous research made by De La Chevalerie *et al.*[19] and De Luca *et al.*[18]

Upon examining streamwise streaks from the side view, the evolution of the streak breakdown process becomes even more apparent in instantaneous Rayleigh scattering images. As shown in Fig. 11(a), the boundary layer remains small variation until $x/L = 1.5$ where a small lift-up vortex can be observed at a low Reynolds number. There is no breakdown process occurring within the FOV. When Reynolds number increases to 7.22×10^5 and 9.19×10^5 [see Figs. 11(b) and 9(c)], the breakdown occurs at around $x/L = 1.35$, agreeing well with the observation in Fig. 10.

In general, the effects of Reynolds number are similar to the effects of ramp angle. Specifically, higher Reynolds numbers result in shorter streamwise streaks that occur at more upstream locations. However, the effect on the spanwise wavelength of the streaks differs from the influence of the ramp angle. As the Reynolds number increases, the spanwise wavelength of streaks decreases slightly.

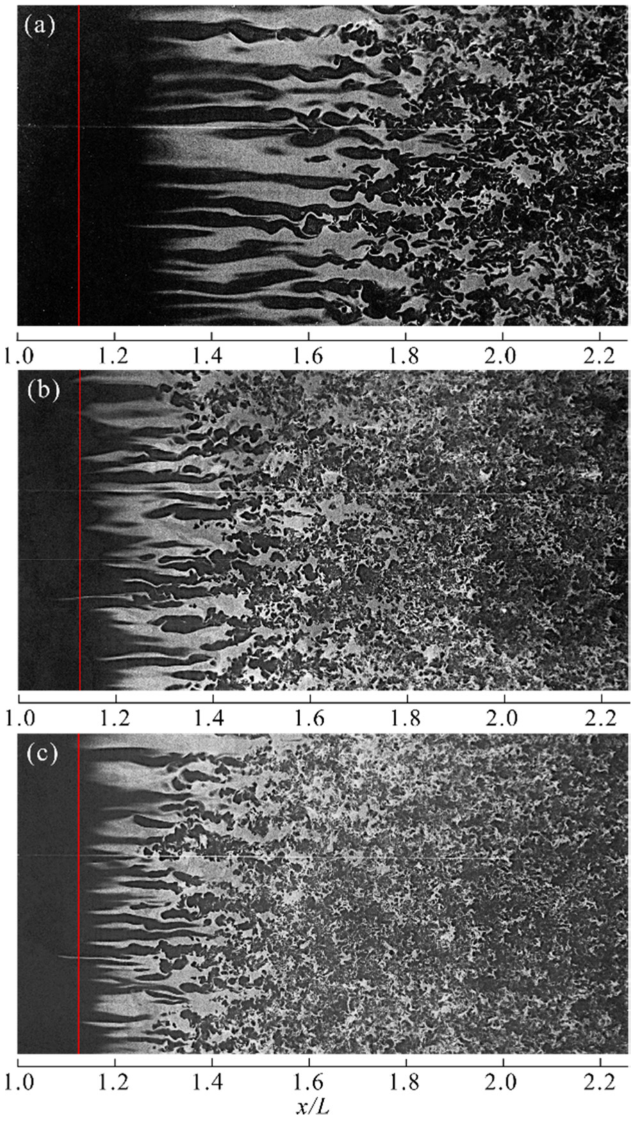

FIG. 10. Rayleigh scattering images at the spanwise view of the ramp plate at (a) $Re_L = 3.66 \times 10^5$, (b) $Re_L = 7.22 \times 10^5$, and (c) $Re_L = 9.19 \times 10^5$, with the ramp angle of 10°. The flow direction is from left to right. The ramp corner is outside the left bound of the image and the red line represents the reattachment region determined by Schlieren images.

C. Discussion on the mechanism of streak breakdown

As aforementioned, the streamwise streaks are associated with the transition process. To examine the evolution and breakdown of streamwise streaks, Fig. 12 shows the zoomed-in views of the images in Fig. 7. The first observation is that the vortex breakdown location varies along the spanwise direction. From repeated experiments, the breakdown process is also shown unsteady. Moreover, the streaks keep slow varying at the beginning, then become twisted prior to the breakdown. The variation of the breakdown location as well as the twisting and stretching behaviors of streaks show the three-dimensional nature of the streaks.

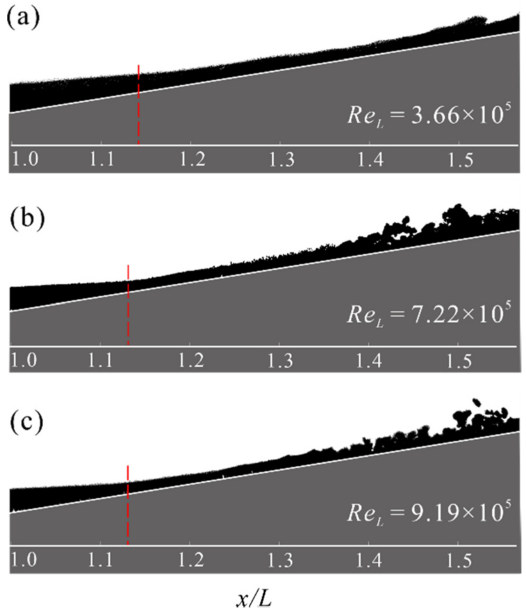

FIG. 11. Rayleigh scattering images on the side view downstream of the corner with (a) $Re_L = 3.66 \times 10^5$, (b) $Re_L = 7.22 \times 10^5$, and (c) $Re_L = 9.19 \times 10^5$. The red dashed line denotes the location of reattachment point determined by Schlieren images.

Second, it can be noticed that when the ramp angle is small, the streaks all exhibit a sinuous shape prior to the breakdown. However, at large ramp angles, a varicose pattern occurs when the local spanwise wavelength become larger, as shown in Figs. 12(c) and 10(d), coexisting with the sinuous pattern. The two patterns observed are similar to those frequently reported in the literature concerning Görtler instability.[3,50,60] Hall and Horseman[61] analytically examined the boundary layer over a curved wall and distinguished two different modes of instability, namely odd mode and even mode, in the breakdown process for Görtler vortices. Later, Li and Malik[60] reported that a sinuous shape of Görtler vortices is promoted by the odd mode, while the even mode results in a varicose shape. They also found that the leading mode depends on the spanwise wavelength of Görtler vortices. The short-wavelength vortices exhibit a preference for the odd mode, while the even mode is stronger at long-wavelength vortices. In the present study, a similar trend is observed, as the wavelength of streaks exhibits unevenness along the spanwise direction. Therefore, the amplification mechanisms of the streamwise streaks in the interaction region may be associated with the Görtler instability. However, Rayleigh scattering images that estimate the region of the boundary layer by the condensation line only exhibit instantaneous flow structures. Also, the scalar tracers could give certain misleading impressions of the flow dynamics.[62] It is not sufficient to identify the presence of the Görtler instability, which needs further numerical investigation.

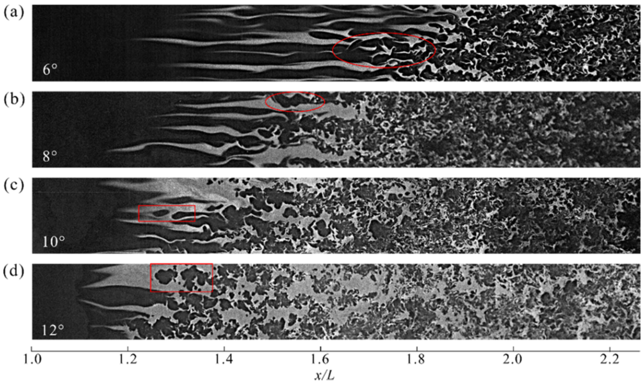

FIG. 12. Detailed structures of streamwise streaks with ramp angles at (a) 6°, (b) 8°, (c) 10°, and (d)12°, at $Re_L = 7.22 \times 10^5$. The rectangle box indicates varicose shape breakdown, and the circle one indicates sinuous shape breakdown.

To further investigate the breakdown process, the PSDs of PCB pressure signals for ramp angles between 6° and 10°, where the length of the streamwise streaks varies significantly, were studied. Figure 13 illustrates PSDs of PCB pressure signals in the corresponding cases. On the flat plate part, all three PSDs show a significant declining trend at low frequency, then keep constant at a low level in the high-

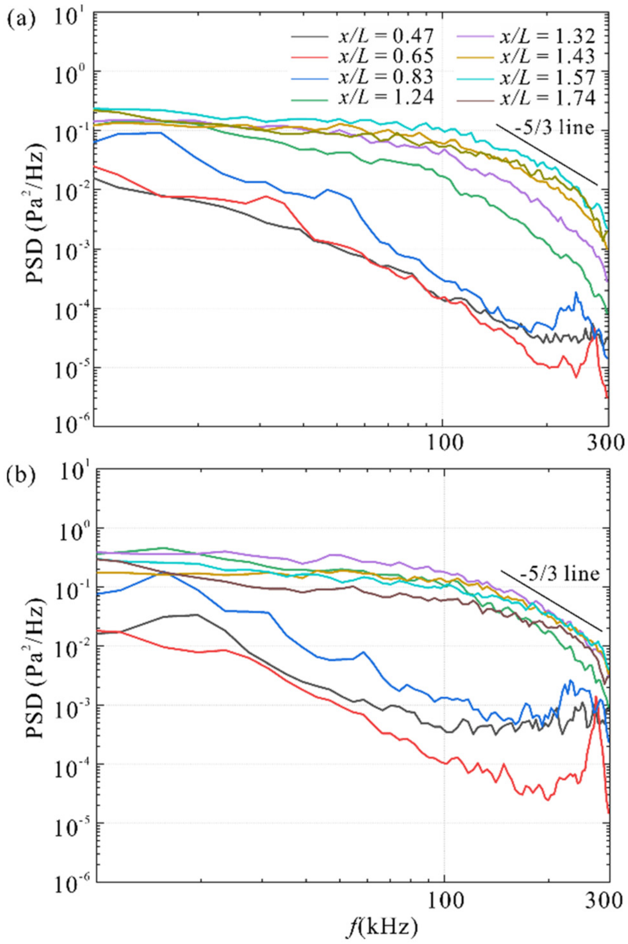

FIG. 13. Power spectral densities of PCB pressure signals along the streamwise direction at (a) 6° and (b) 10° ramp angles with $Re_L = 7.22 \times 10^5$.

TABLE IV. The scaled ramp angle at each test condition.

	Case 1	Case 2	Case 3	Case 4	Case 5	Case 6
α^*	3.6	4.6	4.9	2.7	3.7	5.5

frequency region with only a moderate peak that occurs between 250 and 300 kHz. This peak occurs at relatively low energy and does not belong to any of Mack's modes. In addition, the results of tube tunnel calibration indicate the peak may be part of the background noise. Therefore, no significant Mack's modes are captured in experiments. This may be ascribed to the relatively limited length of the flat plate that may restrict the complete development of Mack's modes within the boundary layer. The noise would embed Mack's modes at the early stage. Similar findings are also reported by Benitez *et al.*[27] Despite that, the flow remains in a laminar state on the flat plate. Therefore, it should not rule out the role of Mack's modes, which will be discussed in detail in Sec. IV D.

Downstream of the reattachment point, distinct patterns of PSDs can be noticed in Figs. 13(a) and 11(b). For the 6° ramp case, the spectra at the high-frequency range have higher energy levels along the streamwise direction and the slope gradually shifts toward the $-5/3$ Kolmogorov roll-off line, indicating that the flow is experiencing the transition process. While at a 10° ramp angle, the transition process completes near $x/L = 1.32$, which indicates the flow is becoming turbulent up there. As discussed earlier, for the 10° ramp angle case, the breakdown of the streaks occurs at around $x/L = 1.4$ [see Fig. 8(c)], which is generally consistent with the PSD results. The same conclusion can be drawn in other cases as well—that the location of the streak breakdown generally matches the location where the PSD results indicates the flow has transitioned to a turbulent state. It is clear now that the transition process is closely associated with the evolution of streamwise streaks. In general, the flow undergoes a transition process in the streak region where streaks persist, then becomes turbulent where the streaks break down. This highlights the important roles that the streamwise streaks play in the transition process in SWBLI.

D. Physics on the formation of streamwise streaks

To further explore the originations of streamwise streaks that appear on the ramp, the GSA and resolvent analysis have been conducted on the 2D base flow to describe the response of the flow to global instability and external forcing, respectively. The comparison of surface pressure coefficient C_p on 2D base flow and experiments (see Fig. 5) shows that a better agreement is achieved in the case with a smaller ramp angle. One possible explanation for the disparity in the size of the separation bubble may be the three-dimensional effects in experiments, which are primarily attributed to the spillage flow at both sides of the corner. In addition, the flows become transitional downstream of the reattachment point (see Fig. 9). In such conditions, the 2D steady solutions cannot predict the transitional flow features. Another difference observed is that the pressure on the ramp is higher than in numerical simulations. This may be due to the additional flow-turning due to the boundary layer and the complex system of shock waves generated by the interactions.[1]

Concerning global instability, Hao *et al.*[7] have established a criterion based on a scaled ramp angle to evaluate the global stability of compression corner flow. The scaled ramp angle, defined with the actual ramp angle α, the Reynolds number Re_L, and the free-stream Mach number M_∞, is based on the triple-deck theory, which was developed by Neiland[63] and Stewartson and Williams.[64] The scaled ramp angle α^* is expressed as follows:

$$\alpha^* = \frac{\alpha Re_L^{1/4}}{C^{1/4} 0.332^{1/2} \left(M_\infty^2 - 1\right)^{1/4}}, \quad C = \frac{\mu_w T_\infty}{\mu_\infty T_w}, \tag{12}$$

where C is the Chapman–Rubesin factor. α^* of each case in the present study is presented in Table IV.

According to the criterion established by Hao *et al.*,[7] the critical scaled ramp angle α^* is at about 4.5, which denotes that the base flows of cases 1, 4, and 5 are globally stable. In addition, based on Eq. (12), the ramp angle α exhibits a greater influence on the change of α^* compared to Reynolds number Re_L, which may indicate a greater potential effect on the flow instability. Figure 14 presents the growth rates of the most unstable mode as a function of spanwise wavelength λ. The stationary modes are denoted by closed circles, indicating modes with an angular frequency of zero, while oscillating modes are denoted by opened circles, indicating modes with a non-zero angular frequency. As shown in Fig. 14(a), the most unstable modes are all stationary modes with negative growth rates for 10° ramp angle and $Re_L = 3.66 \times 10^5$ (case 1). For higher Reynolds number cases, the growth rates reach positive values at peaks, indicating that the flows are globally unstable. At $Re_L = 7.22 \times 10^5$ (case 2), the largest growth rates reach

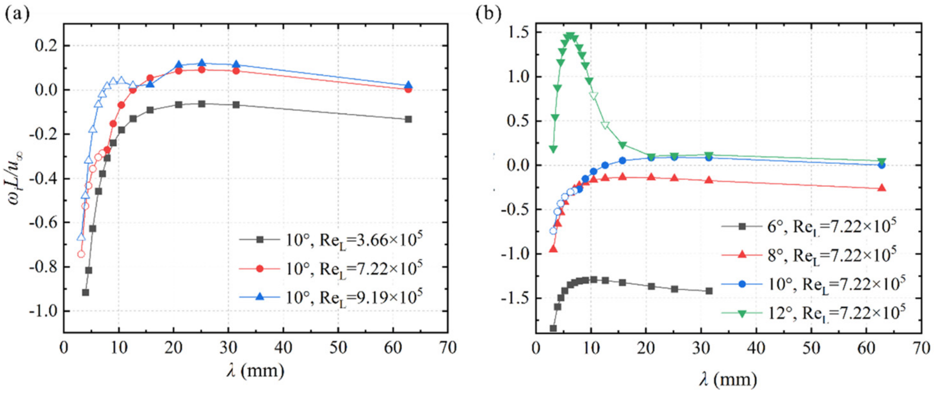

FIG. 14. Growth rates of the most unstable mode as a function of spanwise wavelength for (a) different Reynolds numbers at 10° ramp angle and (b) different ramp angles with $Re_L = 7.22 \times 10^5$. Closed symbols: stationary modes; opened symbols: oscillating modes.

positive values where the spanwise wavelength is around 25 mm. Oscillating modes appear at short wavelengths; however, those modes maintain negative growth rates. At $Re_L = 9.19 \times 10^5$ (case 3), two local peaks occur. The major one corresponds to a stationary mode with the same spanwise wavelength as in cases 1 and 2, while another one manifests as an oscillating mode characterized by a smaller spanwise wavelength, specifically around 9 mm. In the above three cases, the preferential wavelength remains unchanged at 25 mm, which is nearly one order of magnitude larger than observed in experiments. This is mainly because, in GSA, the disturbances are assumed to grow exponentially in time, whereas the actual flow experiences an exponential growth stage followed by a nonlinear saturation stage, eventually reaching a quasi-steady state.[23] Therefore, as discussed in Hao *et al.*,[7] the global instability contributes to the formation of streaks, and the second and higher harmonic modes and their corresponding complex interactions dominate in the quasi-steady state, resulting in a smaller preferential spanwise wavelength, as previously reported by Cao *et al.*[14]

For the 6° and 8° ramp cases (cases 4 and 5), the flows are globally stable, as illustrated in Fig. 14(b). However, two local peaks of the growth rate occur at the 12° ramp case (case 6). The major growth rate occurs when the spanwise wavelength is around 5 mm, which is a stationary mode. Note that the streamwise streaks observed in the globally unstable flow are the results of competition between global and convective instability in experiments, as the effects of convective instability cannot be excluded from globally unstable flow.

Hence, to clearly clarify the role of convection instability, the resolvent analysis is performed to investigate the convective instability under globally stable cases. Figure 15 shows the contours of the optimal gains in the space of βL and ω_r for globally stable cases. Here, the resolvent analysis is employed to investigate the characteristics of convective instability in globally stable cases. Hence, the Reynolds numbers are not the same across different cases. The preferential spanwise wavelength λ_z is then obtained by $\lambda_z = 2\pi/\beta$. Two peaks occur in the contours of all cases. The peak at the low-frequency region is in the form of streamwise streaks, which have been extensively identified by temporal and spatial analyses of transient growth in compressible boundary layers.[65–67] Another local peak is observed on the axis of $\beta L \approx 90$ at $\log_{10}(\omega_r L/u_\infty) \approx 1.4$. This high-frequency optimal response has a non-zero wavenumber, indicating that the disturbance has an oblique wave structure referred to as Mack's first mode.[34] In the literature, Bugeat *et al.*[35] found Mack's first mode, second mode, and the streaks in a supersonic flat-plate boundary layer, while Hao *et al.*[30] identified Mack's second mode and the streaks in a hypersonic compression corner flow, under different conditions. In addition, the highly compressible shear layer is known to exhibit 3D instabilities.[68] Specifically, 3D Kelvin–Helmholtz instability is observed as being amplified in the shear layer of shock-induced separated flows.[29,69] Furthermore, global instability has the potential to support three-dimensional flow bifurcation in a two-dimensional flow.[14] In the present study, resolvent analysis indicates that Mack's first mode and streaks are present in the globally stable flow. No additional three-dimensional modes, such as Kelvin–Helmholtz instability, are detected in the resolvent analysis as well as in experiments. It could be because the optimal gain of those three-dimensional modes is much less than that of Mack's first mode and streaks, or the 3D structures do not develop in this condition.

To be specific, when the ramp angle is 6° (case 4) and 8° (case 5), the maximum optimal gain is associated with Mack's first mode, while the optimal gain of streaks is relatively low but within the same order of magnitude. However, for case 1, the maximum optimal gain of streaks becomes larger than that of Mack's first mode, indicating a switch of the dominant mode of instability. For case 4, the streamwise streaks achieved at around $\beta L = 240$, which denotes that the preferential wavelength is 2.6 mm. The corresponding spanwise wavelengths are 2.4 and 3.5 mm for cases 5 and 1, respectively. As for Mack's first mode, the preferential wavelengths of cases 4 and 5 are all 7.0 mm, while it increases to 9.0 mm in case 1. The preferential wavelength of streaks obtained in the resolvent analysis is much closer to that obtained by experiments. Yet, we cannot rule out the role of Mack's first mode, as it may undergo nonlinear resonance to generate streak structures with twice the wavenumber, which can provide an initial seed of Gortler instability.[70] This nonlinear effect cannot be reflected in linear resolvent analysis. Hence, the streaks identified in the resolvent analysis only imply one possible mechanism for the formation of streaks, which cannot totally represent visualized streaks in the experiments. The summary of the wavelengths of streamwise streaks obtained in experiments, GSA, and resolvent analysis are compared in Table V.

Figure 16 presents the optimal responses and corresponding forcings of the most amplified streamwise streaks at $\omega_r L/u_\infty = 0.01$ in Fig. 13. Concerning the flow response (see the left column in Fig. 16),

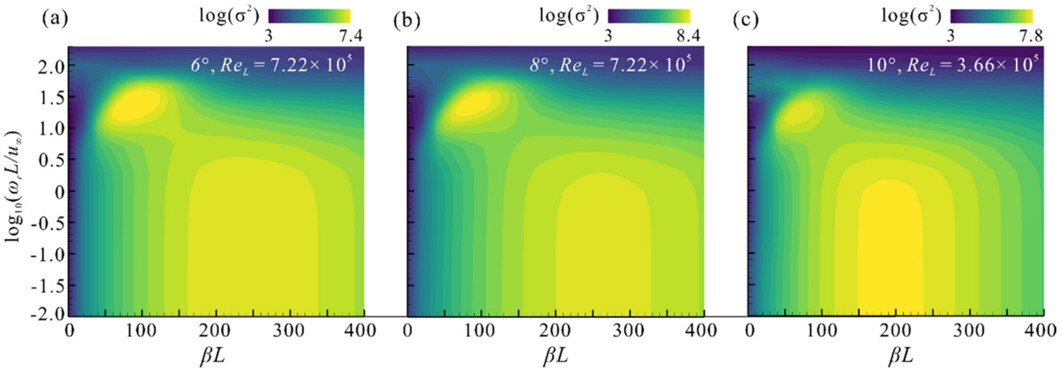

FIG. 15. Contours of optimal gains in the space of spanwise wavenumber and angular frequency for (a) case 4, (b) case 5, and (c) case 1.

TABLE V. Summary of the wavelengths of streamwise streaks obtained in experiments and numerical simulations.

	θ (°)	Re_L ($\times 10^5$)	Exp (mm)	GSA (mm)	Resolvent analysis (mm)
Case1	10	3.66	3.8	25	3.5/9.0
Case2	10	7.22	3.4	25	⋯
Case3	10	9.19	2.9	25	⋯
Case4	6	7.22	3.4	9	2.6/7.0
Case5	8	7.22	3.2	15	2.4/7.0
Case6	12	7.22	3.3	5	⋯

the kinetic energy is contributed mostly by the streamwise velocity perturbation, i.e., $|u'| \gg |v'|$ and $|u'| \gg |w'|$ (not shown here), denoting that the response is in the form of streamwise streaks. Meanwhile, the forcings in all cases are in the form of streamwise vortices with most of the kinetic energy in the wall-normal and spanwise velocity components (see right column in Fig. 16). Such a component-wise energy transfer is usually attributed to the lift-up mechanism.[71] Note that the perturbation is amplified in the shear layer, without interacting with the separation bubble. This indicates that the effect of modal resonance is insignificant.

To illustrate the spatial evolution of the optimal responses of streaks, Fig. 17 shows the Chu energy density integrated in the wall-normal direction along the model surface for the most amplified streamwise streaks. As can be seen in Fig. 17, there are two separate stages of energy growth observed near the separation and reattachment point, especially in Figs. 17(b) and 15(c), where the separation bubble is relatively large. In contrast, the growth is considerably gentle at the corner ($x/L = 1$). The amplification process appears to be associated with separation and reattachment processes, where the flow curvatures are relatively high.

The resolvent analysis reveals that when the flow is globally stable, steady streamwise streaks may originate from the response to external disturbances and Mack's first mode. Concerning the external disturbances, two possible mechanisms may support the formation of streaks. The first one is the transient growth in the flat-plate boundary layer (between the forcing position and the separation point), which is mainly due to the lift-up mechanism. Another one is the significant growth near the separation and reattachment points, which may be associated with Görtler instability. In addition, the nonlinear interaction between two opposite Mack's first modes also has the potential to support the formation of streamwise streaks.

V. CONCLUSION

Experiments were conducted in a Mach 4 Ludwieg tube tunnel to investigate the laminar SWBLI over a compression corner. Schlieren visualization, Rayleigh scattering technique, and surface pressure measurements were employed in the present study. Then, GSA and resolvent analysis were carried out based on a 2D base flow solved by an in-house solver to examine the underlying physics.

Streamwise streaks were observed downstream of the reattachment region using the Rayleigh scattering technique. The evolution

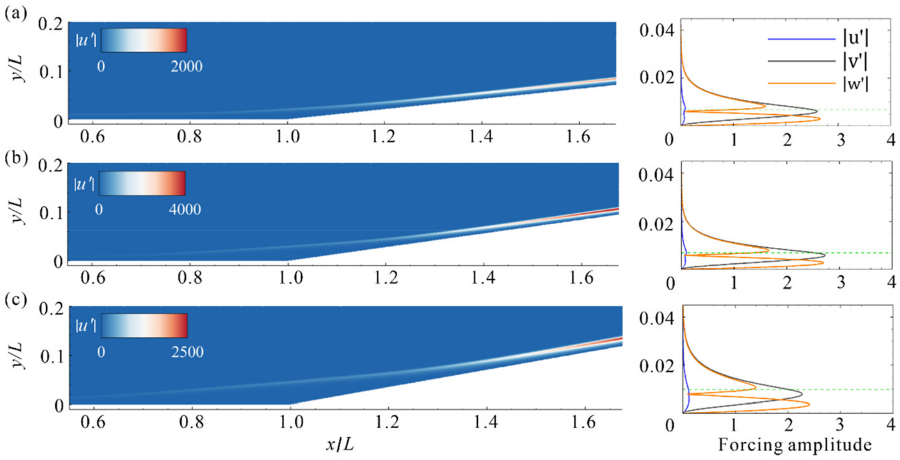

FIG. 16. Optimal responses (left) and the corresponding forcings (right) of the most amplified streamwise streaks for (a) case 4, (b) case 5, and (c) case 1.

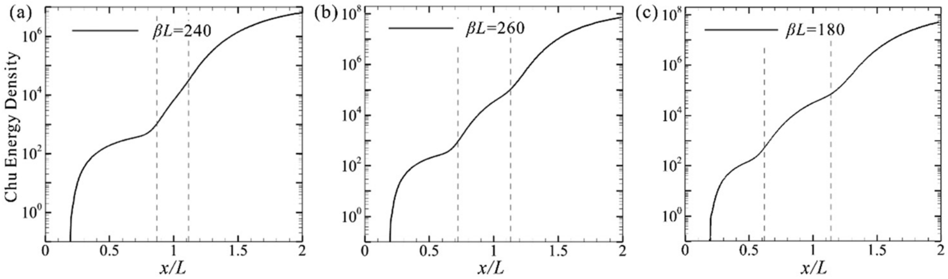

FIG. 17. Distributions of Chu energy density integrated in the wall-normal direction associated with the most amplified streaks for (a) case 4, (b) case 5, and (c) case 1. Dashed lines indicate the separation and reattachment point.

process of streaks, along with detailed flow structures, was also exhibited by plotting streamwise profiles and slices at the boundary layer of the ramp plate. The location where the streaks emerge moves upstream as the ramp angle increases, while the mean length of streaks keeps decreasing. Then, when the Reynolds number is varied at a fixed ramp angle of 10°, a similar trend is noticed. Regarding the wavelength of streaks, it nearly remains constant for different ramp angles, while it decreases when the Reynolds number increases. There are two breakdown patterns observed, which are in sinuous shape and varicose shape. Similar modes are found in the breakdown of Görtler vortices. Clear evidence from pressure measurements and Rayleigh scattering show that the flow is transitional at the streak region and turns turbulent as the streaks break down. Therefore, it can be stated that the laminar–turbulent transition process is associated with the streamwise streaks.

The GSA results show that the flows of cases 1, 4, and 5 are globally stable. However, GSA can only predict the preferential spanwise wavelength in the exponential growth linear stage. Hence, the preferential spanwise wavelength obtained by GSA is not consistent with experiments. In terms of resolvent analysis, two local maxima appear in all globally stable cases, namely Mack's first mode and streaks. The maximum optimal gain of streaks is achieved at a spanwise wavelength range from 2.4 to 3.5 mm, which generally agrees with experimental observation. The preferential spanwise wavelength of Mack's first mode is around 7–9 mm. Although the wavelength is larger, Mack's first mode may undergo nonlinear resonance, generating streak structures with half of the wavelength, as an initial seed of Görtler instability. The distributions of Chu energy density of the most amplified streaks show that the amplification may associated with Görtler instability. However, linear stability analysis and three-dimensional numerical simulation will be employed in future work to further determine the existence of Görtler instability.

ACKNOWLEDGMENTS

The authors are grateful for the financial support provided by the National Natural Science Foundation of China (Nos. 12202374 and 12102377) and the Hong Kong Research Grants Council (Nos. 15216621, 15217622, 15204322, and 25203721).

AUTHOR DECLARATIONS

Conflict of Interest

The authors have no conflicts to disclose.

Author Contributions

Guoqin Zhao: Conceptualization (equal); Data curation (lead); Formal analysis (lead); Methodology (equal); Writing – original draft (lead). **Tianju Ma:** Investigation (equal); Methodology (equal); Project administration (equal). **Zongnan Chen:** Conceptualization (equal); Formal analysis (equal); Project administration (lead). **Zijian Zhang:** Conceptualization (equal); Methodology (equal); Supervision (lead); Writing – review & editing (equal). **Jiaao Hao:** Formal analysis (equal); Supervision (equal); Writing – review & editing (equal). **Chih-Yung Wen:** Conceptualization (equal); Project administration (equal); Supervision (equal); Writing – review & editing (equal).

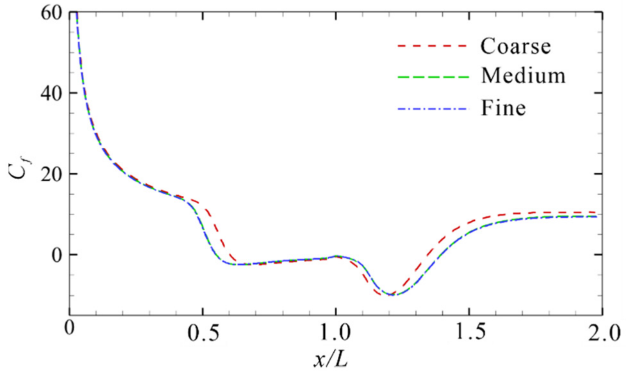

FIG. 18. Distributions of skin friction coefficient obtained by three different levels of grids at a 10° ramp $Re_L = 7.22 \times 10^5$.

DATA AVAILABILITY

The data that support the findings of this study are available from the corresponding author upon reasonable request.

APPENDIX: GRID CONVERGENCE

The computational domain is a classical 2D configuration containing a flat plat and a ramp.[24,30] As the flows become turbulent before $x/L = 2.0$ in all cases, the length of the ramp plate is set to 100 mm to reduce the computational cost. The computational grids are constructed with three levels of grids, which include 600 × 200 (coarse), 800 × 300 (medium), and 1000 × 400 (fine) cells in the streamwise and normal directions. The grid is refined near the separation and reattachment region. The normal spacing at the wall is 2×10^{-7} m to guarantee the grid Reynolds number on the order of magnitude of one at all test conditions. Figure 18 compares the surface distributions of skin friction coefficient C_f obtained in the three levels of grids at a 10° ramp angle with $Re_L = 7.22 \times 10^5$. The skin friction coefficient C_f is defined by

$$C_f = \frac{\tau_w}{0.5\rho_\infty u_\infty^2}, \tag{A1}$$

where τ_w is the surface shear stress. The results indicate that the medium level of grids is enough to ensure grid independence.

REFERENCES

[1] H. Babinsky and J. K. Harvey, *Shock Wave-Boundary-Layer Interactions* (Cambridge University Press, 2011).
[2] D. V. Gaitonde, "Progress in shock wave/boundary layer interactions," Prog. Aerosp. Sci. **72**, 80–99 (2015).
[3] C. Lee and X. Jiang, "Flow structures in transitional and turbulent boundary layers," Phys. Fluids **31**, 111301 (2019).
[4] J. Fan, J. Hao, and C.-Y. Wen, "Nonlinear interactions of global instabilities in hypersonic laminar flow over a double cone," Phys. Fluids **34**, 126108 (2022).
[5] J. Hao, J. Fan, S. Cao, and C.-Y. Wen, "Three-dimensionality of hypersonic laminar flow over a double cone," J. Fluid Mech. **935**, A8 (2022).
[6] A. Roghelia, H. Olivier, I. Egorov, and P. Chuvakhov, "Experimental investigation of Görtler vortices in hypersonic ramp flows," Exp. Fluids **58**, 139 (2017).
[7] J. Hao, S. Cao, C.-Y. Wen, and H. Olivier, "Occurrence of global instability in hypersonic compression corner flow," J. Fluid Mech. **919**, A4 (2021).

[8] M. Lugrin *et al.*, "Transitional shockwave/boundary layer interaction experiments in the R2Ch blowdown wind tunnel," Exp. Fluids **63**, 46 (2022).

[9] H. G. Hornung, R. J. Gollan, and P. A. Jacobs, "Unsteadiness boundaries in supersonic flow over double cones," J. Fluid Mech. **916**, A5 (2021).

[10] Z. Song and J. Hao, "Global instability of the interaction between an oblique shock and a laminar boundary layer," Phys. Fluids **35**, 084121 (2023).

[11] A. Dwivedi, N. Hildebrand, J. W. Nichols, G. V. Candler, and M. R. Jovanović, "Transient growth analysis of oblique shock wave/boundary-layer interactions at Mach 5.92," Phys. Rev. Fluids **5**, 063904 (2020).

[12] R. Benay, B. Chanetz, B. Mangin, L. Vandomme, and J. Perraud, "Shock wave/transitional boundary-layer interactions in hypersonic flow," AIAA J. **44**, 1243 (2006).

[13] C. Li and J. Hao, "Global stability of supersonic flow over a hollow cylinder/flare," J. Fluid Mech. **975**, A40 (2023).

[14] S. Cao, J. Hao, I. Klioutchnikov, H. Olivier, and C.-Y. Wen, "Unsteady effects in a hypersonic compression ramp flow with laminar separation," J. Fluid Mech. **912**, A3 (2021).

[15] J. J. Ginoux, "On some properties of reattaching laminar and transitional high speed flows," Technical Report No. TN 53. Von Kármán Institute, 1969, see https://apps.dtic.mil/sti/citations/AD0860313.

[16] G. Simeonides and W. Haase, "Experimental and computational investigations of hypersonic flow about compression ramps," J. Fluid Mech. **283**, 17–42 (1995).

[17] M. Lugrin, S. Beneddine, C. Leclercq, E. Garnier, and R. Bur, "Transition scenario in hypersonic axisymmetrical compression ramp flow," J. Fluid Mech. **907**, A6 (2021).

[18] L. De Luca, G. Cardone, D. A. De La Chevalerie, and A. Fonteneau, "Viscous interaction phenomena in hypersonic wedge flow," AIAA J. **33**, 2293–2298 (1995).

[19] D. A. De La Chevalerie, A. Fonteneau, L. De Luca, and G. Cardone, "Görtler-type vortices in hypersonic flows: The ramp problem," Exp. Therm. Fluid Sci. **15**, 69–81 (1997).

[20] E. Reshotko, "Transition issues for atmospheric entry," J. Spacecr. Rockets **45**, 161–164 (2008).

[21] L. M. Mack, "Linear stability theory and the problem of supersonic boundary-layer transition," AIAA J. **13**, 278–289 (1975).

[22] C. Whang and X. Zhong, "Secondary Görtler instability in hypersonic boundary layers," AIAA Paper No. AIAA 2001-273, 2001.

[23] J.-C. Robinet, "Bifurcations in shock-wave/laminar-boundary-layer interaction: Global instability approach," J. Fluid Mech. **579**, 85–112 (2007).

[24] S. Cao *et al.*, "Transition to turbulence in hypersonic flow over a compression ramp due to intrinsic instability," J. Fluid Mech. **941**, A8 (2022).

[25] N. Hildebrand, A. Dwivedi, J. W. Nichols, M. R. Jovanović, and G. V. Candler, "Simulation and stability analysis of oblique shock-wave/boundary-layer interactions at Mach 5.92," Phys. Rev. Fluids **3**, 013906 (2018).

[26] P. Huerre and P. A. Monkewitz, "Local and global instabilities in spatially developing flows," Annu. Rev. Fluid Mech. **22**, 473–537 (1990).

[27] E. K. Benitez, S. Esquieu, J. S. Jewell, and S. P. Schneider, "Instability measurements on an axisymmetric separation bubble at Mach 6," AIAA Paper No. AIAA 2020-3072, 2020.

[28] P. Balakumar, H. Zhao, and H. Atkins, "Stability of hypersonic boundary layers over a compression corner," AIAA J. **43**, 760–767 (2005).

[29] F. Guiho, F. Alizard, and J.-C. Robinet, "Instabilities in oblique shock wave/laminar boundary-layer interactions," J. Fluid Mech. **789**, 1–35 (2016).

[30] J. Hao, S. Cao, P. Guo, and C.-Y. Wen, "Response of hypersonic compression corner flow to upstream disturbances," J. Fluid Mech. **964**, A25 (2023).

[31] S. Navarro-Martinez and O. R. Tutty, "Numerical simulation of Görtler vortices in hypersonic compression ramps," Comput. Fluids **34**, 225–247 (2005).

[32] S. S. Sawant, V. Theofilis, and D. A. Levin, "On the synchronisation of three-dimensional shock layer and laminar separation bubble instabilities in hypersonic flow over a double wedge," J. Fluid Mech. **941**, A7 (2022).

[33] A. Dwivedi, G. S. Sidharth, J. W. Nichols, G. V. Candler, and M. R. Jovanović, "Reattachment streaks in hypersonic compression ramp flow: An input-output analysis," J. Fluid Mech. **880**, 113–135 (2019).

[34] L. M. Mack, "Boundary-layer linear stability theory," AGARD Report. No. 709 (1984).

[35] B. Bugeat, J.-C. Chassaing, J.-C. Robinet, and P. Sagaut, "3D global optimal forcing and response of the supersonic boundary layer," J. Comput. Phys. **398**, 108888 (2019).

[36] E. K. Benitez *et al.*, "Instability and transition onset downstream of a laminar separation bubble at Mach 6," J. Fluid Mech. **969**, A11 (2023).

[37] S. E. M. Niessen, K. J. Groot, S. Hickel, and V. E. Terrapon, "Convective instabilities in a laminar shock-wave/boundary-layer interaction," Phys. Fluids **35**, 024101 (2023).

[38] C. S. Butler and S. J. Laurence, "Transitional hypersonic flow over slender cone/flare geometries," J. Fluid Mech. **949**, A37 (2022).

[39] P. Paredes *et al.*, "Boundary-layer instabilities over a cone–cylinder–flare model at Mach 6," AIAA J. **60**, 5652–5661 (2022).

[40] Z. Chen, J. Hao, and C.-Y. Wen, "Control of supersonic compression corner flow using a plasma actuator," Phys. Fluids **34**, 073605 (2022).

[41] E. N. A. Hoffman *et al.*, "Flow characterization of the UTSA hypersonic Ludwieg tube," Aerospace **10**, 463 (2023).

[42] K. P. Bearden, V. E. Padilla, L. Taubert, and S. A. Craig, "Calibration and performance characterization of a Mach 5 Ludwieg tube," Rev. Sci. Instrum. **93**, 085104 (2022).

[43] F. Munoz *et al.*, "Freestream disturbances characterization in Ludwieg tubes at Mach 6," AIAA Paper No. AIAA 2019-0878, 2019.

[44] J. Threadgill *et al.*, "Scaling and transition effects on Hollow-Cylinder/Flare SBLIs in wind tunnel environments," AIAA Paper No. AIAA 2024-0498, 2024.

[45] G. Simeonides, *Hypersonic Shock Wave Boundary Layer Interactions over Compression Corners* (University of Bristol, 1992).

[46] P. V. Chuvakhov *et al.*, "Effect of small bluntness on formation of Görtler vortices in a supersonic compression corner flow," J. Appl. Mech. Tech. Phys. **58**, 975–989 (2017).

[47] D. J. Ort and J. J. Dosch, "Influence of mounting on the accuracy of piezoelectric pressure measurements for hypersonic boundary layer transition," AIAA Paper No. AIAA 2019-2292 (2019).

[48] J. A. S. Threadgill, J. C. Little, and S. H. Wernz, "Transitional shock boundary layer interactions on a compression ramp at Mach 4," AIAA J. **59**, 4824–4841 (2021).

[49] C. Zhang and C. Lee, "Rayleigh-scattering visualization of the development of second-mode waves," J. Visualization **20**, 7–12 (2017).

[50] G. Huang, W. Si, and C. Lee, "Inner structures of Görtler streaks," Phys. Fluids **33**, 034116 (2021).

[51] P. Erbland *et al.*, "Development of planar diagnostics for imaging Mach 8 flowfields using carbon dioxide and sodium seeding," AIAA Paper No. AIAA 1997-154, 1997).

[52] D. Sorensen, R. Lehoucq, C. Yang, and K. Maschhof, see https://epubs.siam.org/doi/book/10.1137/1.9780898719628 for more information about ARPACK software (1996–2008).

[53] X. S. Li, J. W. Demmel, J. R. Gilbert, and L. Grigori, see https://scholar.google.com/citations?view_op=view_citation&hl=zh-TW&user=Bjpb27sAAAAJ&citation_for_view=Bjpb27sAAAAJ:ULOm3_A8WrAC for more information about SuperLU User's Guide. Technical Report No. LBNL-44289, 1999.

[54] B.-T. Chu, "On the energy transfer to small disturbances in fluid flow (Part I)," Acta Mech. **1**, 215–234 (1965).

[55] S. L. Gai and A. Khraibut, "Hypersonic compression corner flow with large separated regions," J. Fluid Mech. **877**, 471–494 (2019).

[56] K. Heffner, A. Chpoun, and J. Lengrand, "Experimental study of transitional axisymmetric shock-boundary layerinteractions at Mach 5," AIAA Paper No. AIAA 1993-3131, 1993.

[57] Y. Zhuang, H. J. Tan, Y. Z. Liu, Y. C. Zhang, and Y. Ling, "High resolution visualization of Görtler-like vortices in supersonic compression ramp flow," J. Visualization **20**, 505–508 (2017).

[58] X. Y. Jiang, C. B. Lee, C. R. Smith, J. W. Chen, and P. F. Linden, "Experimental study on low-speed streaks in a turbulent boundary layer at low Reynolds number," J. Fluid Mech. **903**, A6 (2020).

[59] X. Y. Jiang, C. B. Lee, X. Chen, C. R. Smith, and P. F. Linden, "Structure evolution at early stage of boundary-layer transition: Simulation and experiment," J. Fluid Mech. **890**, A11 (2020).

[60] F. Li and M. R. Malik, "Fundamental and subharmonic secondary instabilities of Görtler vortices," J. Fluid Mech. **297**, 77–100 (1995).

[61] P. Hall and N. J. Horseman, "The linear inviscid secondary instability of longitudinal vortex structures in boundary layers," J. Fluid Mech. **232**, 357 (1991).

[62] J. M. Cimbala, H. M. Nagib, and A. Roshko, "Large structure in the far wakes of two-dimensional bluff bodies," J. Fluid Mech. **190**, 265–298 (1988).

[63] V. Y. Neiland, "Theory of laminar boundary layer separation in supersonic flow," Fluid Dyn. **4**, 33–35 (1969).
[64] K. Stewartson and P. G. Williams, "Self-induced separation," Proc. R. Soc. London, Ser. A **312**, 181206 (1969).
[65] P. Andersson, M. Berggren, and D. S. Henningson, "Optimal disturbances and bypass transition in boundary layers," Phys. Fluids **11**, 134–150 (1999).
[66] A. Tumin and E. Reshotko, "Optimal disturbances in compressible boundary layers," AIAA Paper No. AIAA 2003-792, 2003.
[67] D. Tempelmann, A. Hanifi, and D. S. Henningson, "Spatial optimal growth in three-dimensional compressible boundary layers," J. Fluid Mech. **704**, 251–279 (2012).
[68] N. D. Sandham and W. C. Reynolds, "Three-dimensional simulations of large eddies in the compressible mixing layer," J. Fluid Mech. **224**, 133–158 (1991).
[69] O. Tumuklu, V. Theofilis, and D. A. Levin, "On the unsteadiness of shock–laminar boundary layer interactions of hypersonic flows over a double cone," Phys. Fluids **30**, 106111 (2018).
[70] P. Guo, J. Hao, and C.-Y. Wen, "Interaction and breakdown induced by multiple optimal disturbances in hypersonic boundary layer," J. Fluid Mech. **974**, A50 (2023).
[71] M. T. Landahl, "A note on an algebraic instability of inviscid parallel shear flows," J. Fluid Mech. **98**, 243–251 (1980).